



HAL
open science

A Possible Dust Origin for an Unusual Feature in Io's Sodium Neutral Clouds

Cesare Grava, Timothy Cassidy, Nicholas M. Schneider, Hsiang-Wen Hsu, Jeffrey P. Morgenthaler, François Leblanc, Valeria Mangano, Kurt D. Retherford, Matthew H. Burger, Cesare Barbieri

► **To cite this version:**

Cesare Grava, Timothy Cassidy, Nicholas M. Schneider, Hsiang-Wen Hsu, Jeffrey P. Morgenthaler, et al.. A Possible Dust Origin for an Unusual Feature in Io's Sodium Neutral Clouds. *The Astronomical Journal*, 2021, 162 (5), pp.190. 10.3847/1538-3881/ac1ff8 . insu-03374890

HAL Id: insu-03374890

<https://insu.hal.science/insu-03374890>











Submitted on 1 Nov 2021

HAL is a multi-disciplinary open access archive for the deposit and dissemination of scientific research documents, whether they are published or not. The documents may come from teaching and research institutions in France or abroad, or from public or private research centers.

L'archive ouverte pluridisciplinaire **HAL**, est destinée au dépôt et à la diffusion de documents scientifiques de niveau recherche, publiés ou non, émanant des établissements d'enseignement et de recherche français ou étrangers, des laboratoires publics ou privés.

Copyright

A possible dust origin for an unusual feature in Io's sodium neutral clouds

2 CESARE GRAVA ¹, TIMOTHY A. CASSIDY ², NICHOLAS M. SCHNEIDER ², HSIANG-WEN HSU ²,
3 JEFFREY P. MORGENTHALER ³, FRANÇOIS LEBLANC ⁴, VALERIA MANGANO ⁵, KURT D. RETHERFORD ^{1,6},
4 MATTHEW H. BURGER ⁷ AND CESARE BARBIERI ⁸

5 ¹*Southwest Research Institute, 6220 Culebra road, San Antonio, TX, 78238, USA*

6 ²*Laboratory for Atmospheric and Space Physics, University of Colorado Boulder, Boulder, CO, USA*

7 ³*Planetary Science Institute, Tucson, AZ, USA*

8 ⁴*LATMOS/CNRS, Sorbonne Université, UVSQ, IPSL, Paris, France*

9 ⁵*INAF/IAPS, Rome, Italy*

10 ⁶*University of Texas at San Antonio, San Antonio, TX, USA*

11 ⁷*Space Telescope Science Institute, Baltimore, MD, USA*

12 ⁸*University of Padua, Department of Physics and Astronomy, Padua, Italy*

13 (Received June 1, 2019; Revised January 10, 2019; Accepted July 1, 2021)

14 Submitted to AJ

15 ABSTRACT

16 We report the results of model simulations performed to explain the nature of a sodium emission
17 feature in Io Neutral Clouds. The feature was detected via high-resolution spectroscopic observations
18 from the 3.6-meter Italian telescope TNG. The emission feature is blueshifted compared to the main
19 emission (the banana-shaped Neutral Cloud of Io) by a few tens of km s⁻¹, and it is most prominent
20 when Io is a few tens of degrees before eclipse behind Jupiter's shadow. The feature's morphology
21 changes with time, indicative of a geometrical effect. We constrained its direction, velocity, and column
22 density with a model of sodium atom trajectories under the influence of Io's and Jupiter's gravity and
23 solar radiation pressure. The model that best explains this emission feature has the atoms injected into
24 the exosphere from the leading/sub-Jovian hemisphere of Io (45-68° West longitude), with velocities
25 from 50 to 90 km s⁻¹ relative to Io. These trajectories are consistent with those of negatively charged
26 dust grains (radius ~10 nm) accelerated by the co-rotational electric field of Jupiter's magnetosphere.
27 We propose that sputtering of sodium atoms from Na-bearing molecules (NaCl and Na₂SO₄) in these
28 nanodust grains is the process responsible for our emission feature. Both modeling and observational
29 constraints provide an order-of-magnitude estimate of the sodium production rate of ~10²⁶ s⁻¹. Our
30 work provides another method to monitor the amount of material that Io is supplying to its Neutral
31 Clouds and plasma torus.

32 *Keywords:* (not needed now)

33 1. INTRODUCTION

34 Io's Neutral Clouds are one of the brightest visible
35 manifestations of the intense volcanic and magneto-
36 spheric activity in the Jovian system. All the material
37 that fills the Io Plasma Torus and Io's Neutral Clouds
38 ultimately comes from the intense volcanic activity of

39 Io. Since the discovery of sodium at Io (Brown 1974),
40 and its Neutral Cloud (Trafton et al. 1974), this mi-
41 nor but bright species has been used to monitor the re-
42 sponse of Io's Neutral Cloud to the changes of its drivers
43 (Io volcanic activity and Jupiter magnetosphere). The
44 resonant scattering efficiency (the so-called g-value) of
45 sodium is orders of magnitude greater than the domi-
46 nant species in Io's Neutral Clouds (S and O and their
47 molecular compounds). Moreover, the wavelength of the
48 sodium doublet (the D2 line at D1 line around 5900 Å)
49 is such that it can be easily detected from the ground.

Over the past decades, observations and models have identified structures in the Neutral Clouds, each related to a particular source process and interaction with the Jovian magnetosphere. The most prominent of these structures, and the first to be discovered, is the corona, sometimes referred to as the “banana cloud” (the “Region B” in [Brown et al. 1975](#)), composed of slowly escaping sodium atoms (a few km s^{-1} relative to Io). Its peculiar morphology, with the leading part more extended (about 60° along the orbit) than the trailing part (30° along the orbit), is controlled by celestial mechanics and by ionization from the plasma torus, which is warmer outwards from Io’s orbit compared to inwards ([Nash et al. 1986](#)). Another feature of the sodium Neutral Clouds is the “jet” (or directional feature; [Goldberg et al. 1984](#)), much more variable than the banana cloud, and composed of much more energetic atoms. The “jet” extends from Io in the anti-Jupiter direction, oriented approximately perpendicularly to the local Jovian magnetic field ([Wilson & Schneider 1994](#)). It is probably caused by prompt pickup ion neutralization very close to Io, its narrowness indicating an unperturbed Jovian magnetic field at Io ([Wilson & Schneider 1999](#)). The outer acceleration results from the corotational electric field applied to positively charged ions. Finally, a more diffuse feature is the “stream” ([Schneider et al. 1991](#)) of fast moving neutral sodium atoms resulting from dissociative recombination of fast molecular sodium-bearing ions (most likely NaCl^+) corotating with Jupiter at $\sim 70 \text{ km s}^{-1}$. These atoms can be found all around Io’s orbit. Over many orbits around Jupiter, this stream creates the vast, faint neutral sodium cloud detected hundreds of Jupiter radii from Jupiter ([Mendillo et al. 1990](#)). All these features contribute to the roughly 1 ton of plasma that is injected in the Io Plasma Torus every second ([Schneider & Bagenal 2007](#)). Their morphology depends on several factors, including Io’s position (both orbital longitude and magnetic latitude) Jupiter’s magnetic field, and Io’s volcanic activity (see review by [Bagenal & Dols 2020](#)). For example, it has long been debated whether the sodium Neutral Clouds decrease in extent during eclipses behind Jupiter, due to condensation of Io’s atmosphere and/or to a suppression of solar photons available for photodissociation of sodium-bearing molecular compounds. It was to test these possibilities that we performed ground-based observations of Io before and after eclipses, in 2007. We discovered that solar flux is an important factor in supplying the sodium atoms to the Neutral Clouds, and that suppression of photo-dissociation of sodium-bearing molecules (most likely NaCl) during eclipse drives a decrease in exospheric Na atoms soon after egress ([Grava et al. 2014](#)).

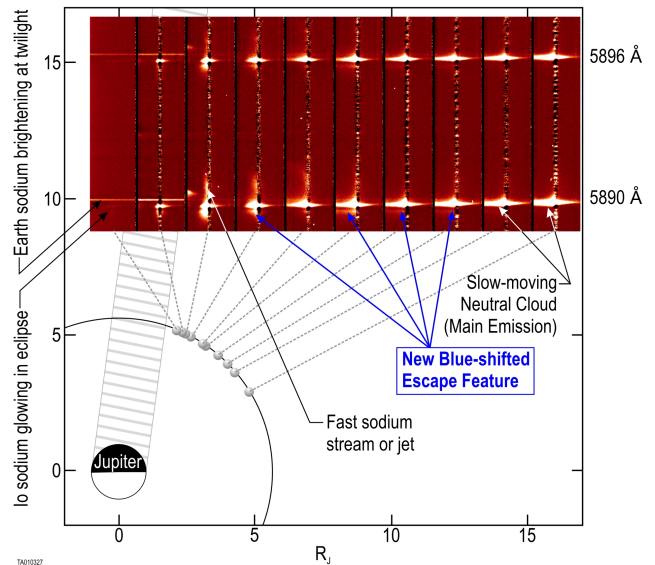


Figure 1. Two-dimensional spectra of Io with the continuum subtracted, stacked over a scheme of the observational geometry. The spectra progress in time from right to left, and wavelength run from bottom to top. The width of the spectra, corresponding to the length of the slit, is 27 arcsec. R_J = Jupiter radius $\sim 70,000 \text{ km}$. In the spectra, Jupiter direction is to the left of Io’s subtracted continuum.

During those observing runs, we also discovered an additional spectroscopic feature: an emission of sodium (visible at both D-lines) blueshifted (i.e., directed towards the observer and thus towards Jupiter) by tens of km s^{-1} relative to Io, hence moving much faster than the escape speed at Io (see Figure 1). We first reported this feature in [Schneider et al. \(2008\)](#) and performed additional observations at the same telescope in 2009. This paper describes the analysis of this feature using simulations of sodium atoms in Io’s Neutral Clouds and suggests possible explanations.

2. OBSERVATIONS AND DATA REDUCTION

Spectra were collected by the now-decommissioned high-resolution échelle spectrograph SARG mounted at the 3.6-meter Italian telescope TNG (Telescopio Nazionale Galileo) during several nights spanning 2 years, and different geometric configurations of Io. Spectra taken in 2007 were analyzed by [Grava et al. \(2014\)](#) and included in this work for completeness, while spectra taken in 2009 are analyzed here for the first time. The spectrograph’s slit was 26.7-arcsec long and 0.4-arcsec wide, had a spectral resolution of $\lambda/\Delta\lambda \sim 115,000$, and was placed almost always parallel to Jupiter’s rotational equator and centered on Io (or on other Galilean satellites, when used for calibration). The exposure time was almost always 600 s. The 2007 spectra were ob-

129 tained with an interference filter which blocked all pho-
 130 tons but those with wavelengths close to the sodium
 131 doublet. This procedure allowed to use the full extent
 132 of the long slit without order overlapping. The 2009
 133 spectra were obtained without such interference filter,
 134 to collect light from the entire bandpass of SARG (3700-
 135 10,000 Å) and to study therefore other species. As such,
 136 only the central ~ 50 pixels were used, and the remain-
 137 ing ~ 30 pixels at the edges were excluded due to order
 138 contamination. The effective length of the slit in this
 139 case was 17.7 arcsec.

140 Data reduction of the spectra was described in depth
 141 in Grava et al. (2014) and is summarized here. Stan-
 142 dard data reduction steps such as subtraction of bias,
 143 flatfielding, and wavelength calibration (using a Th-Ar
 144 lamp) were performed using IRAF routines. Specific
 145 data reduction steps pertinent to our dataset were per-
 146 formed later and included: 1) removal of an interference
 147 pattern caused by the sodium filter (for 2007 observa-
 148 tions only); 2) removal of a “pedestal” (residual back-
 149 ground); 3) removal of a “ghost” of Jupiter’s spectrum
 150 on top of Io spectra; 4) removal of telluric absorption,
 151 performed using rapidly rotating O- and B-type stars
 152 devoid of absorption lines observed at several airmasses
 153 that bracketed ours; 5) subtraction of the “continuum”,
 154 i.e. the solar light reflected off Io’s disk using spectra of
 155 other Galilean satellites (Europa, Ganymede, and, more
 156 rarely, Callisto) properly shifted to account for the dif-
 157 ferent Doppler speeds; 6) conversion of sodium bright-
 158 ness from counts s^{-1} to Rayleighs ($1 \text{ R} = 10^6/4\pi$ photons
 159 $\text{cm}^{-2} \text{ s}^{-1} \text{ sr}^{-1}$; Hunten et al. (1956)) using Jupiter spec-
 160 tra and the well-measured intrinsic brightness of Jupiter
 161 at the sodium wavelength ($5.5 \text{ MR } \text{Å}^{-1}$; Brown & Schnei-
 162 der 1981). During most of the nights the seeing was
 163 good, never exceeding 1.6 arcsec as FWHM (calculated
 164 as a deconvolution of a Gaussian fit to Io’s continuum
 165 and the theoretical diameter of Io’s disk, 1.2 arcsec).
 166 Details of observations are summarized in Table 1.

168 3. THE BLUESHIFTED EMISSION FEATURE

169 Figure 2 shows a typical spectrum of Io. On the left
 171 is the average of Io’s brightness over detector columns
 172 31-33, corresponding to a distance of 1.7-2.9 R_{Io} east-
 173 wards on the sky plane (towards Jupiter, in this case)
 174 of Io’s center ($1 R_{\text{Io}} \sim 1820 \text{ km}$) and, in dashed line,
 175 the g-values. The g-value (or g-factor) is the number of
 176 solar photons resonantly scattered each second by each
 177 sodium atom. In optically thin exospheres, like Io’s neu-
 178 tral clouds, the brightness I (in Rayleighs) is directly
 179 related to the line-of-sight column density N (in atoms
 180 cm^{-2}) by the g-value g (Brown & Yung 1976):

$$I = g \cdot N \quad (1)$$

181 The g-value (expressed in photons atoms $^{-1} \text{ s}^{-1}$) is related
 182 to the solar spectrum, and depends, among other things,
 183 on the heliocentric radial velocity Δv of sodium atoms,
 184 owing to the deep Fraunhofer absorption in the solar
 185 spectrum Hunten et al. (1988). We used g-values for
 186 sodium from Killen et al. (2009). Δv is measured in
 187 our spectra by the Doppler shift $\Delta\lambda$ of Io relative to the
 188 reference wavelengths λ of the sodium D-lines (5889.95
 189 and 5895.92 Å for the D2 and D1 line, respectively):

$$\Delta v = c \cdot \frac{\Delta\lambda}{\lambda} \quad (2)$$

190 where c is the speed of light. The resulting Δv is referred
 191 to Io’s reference frame, which is in itself moving relative
 192 to the Sun. An atom at rest at Io moving away from the
 193 Sun (like at Western elongations) will “see” a redshifted
 194 solar spectrum. Therefore, to properly convert bright-
 195 ness into column densities it is necessary to blueshift the
 196 g-values, i.e. shifting them towards negative velocities.
 197 This is shown in Figure 2, panel a, which shows that
 198 the “dip” in the emission line (in Rayleighs) at -5 km
 199 s^{-1} is caused by the “dip” of the Fraunhofer line of the
 200 g-value at -2.5 km s^{-1} . The resulting division gives the
 201 column density without such “dip” (panel b), but with
 202 a “bump” on the blue side of the peak (negative veloci-
 203 ties). This is the new emission feature. It is reminiscent
 204 of the “skirt” detected first by Trafton (1975) and then
 205 by Cremonese et al. (1992) and interpreted by Trafton &
 206 Macy (1977, 1978) to be due to sodium atoms streaming
 207 away from Io at moderate speeds (18 km s^{-1} at most)
 208 in the leading direction. However, it is different from
 209 that because the “bump” lies on the opposite side. Our
 210 “bump” is more prominent on the short wavelength side
 211 when Io is west of Jupiter. Moreover, as we shall see
 212 briefly, the feature changes Doppler shift through the
 213 night. Note that in our observations the West direction
 214 corresponds to the orbital trailing side of Io. In terms
 215 of plasma flow, the trailing side corresponds to the is
 216 upstream side, and East is the leading (or downstream)
 217 side.

218 We performed the conversion from brightness to col-
 219 umn density for all of our 2D spectra. An example of
 220 the resulting 2D spectra, together with the geometry of
 221 the observation, is shown in Figure 3 (the others can be
 222 found in the supplemental material). In this figure, Io
 223 is about to enter Jupiter’s shadow and the main emis-
 224 sion feature (the “banana cloud”), being approximately
 225 at rest relative to Io (white horizontal dashed lines),
 226 dominates the spectra. The faint, straight emission line
 227 traversing the whole slit length is Earth’s sodium layer
 228 at 90 km altitude resonantly scattering solar photons
 229 shortly before dawn. The streak of diffuse emission very
 230 close to Io on the Eastern side (negative R_{Io}) extending
 231

Table 1. List of observations. t = exposure time. ssl = subsolar longitude, counted Westward (or counterclockwise) on Io. It is also equivalent to Io's orbital longitude, with 0° corresponding to superior conjunction (Io opposite to Earth behind Jupiter) and 90° corresponding to Eastern elongation. λ_{III} and $Mlat$ are Io's system III longitude and magnetic latitude, respectively. $p.a.$ = position angle, or the slit's angle relative to Jupiter's rotation axis, counted counterclockwise starting from Jupiter's north pole.

filename	obs. mid-time (UT)	t (s)	ssl ($^\circ$)	λ_{III} ($^\circ$)	$Mlat$ ($^\circ$)	$p.a.$ ($^\circ$)
JDEI0102	2007-04-25T02:01:33	600	316	29	-10	66
JDEI0106	2007-04-25T03:07:52	600	326	59	-8	66
JDEI0109	2007-04-25T03:39:07	600	330	74	-6	66
JDEI0112	2007-04-25T04:14:26	600	335	90	-4	66
JDEI0114	2007-04-25T04:50:26	600	340	107	-1	66
JDEI0115	2007-04-25T05:02:42	600	342	112	0	66
JDEI0119	2007-04-25T05:41:37	600	347	130	3	90
JDEI0120	2007-04-25T05:53:17	600	349	136	4	90
JDEI0121	2007-04-25T06:04:55	600	351	141	5	90
JDEI0122	2007-04-25T06:12:44	120	352	146	5	90
JDWF0002	2007-05-11T00:16:32	600	316	213	9	85
JDWF0004	2007-05-11T00:39:57	600	319	223	9	90
JDWF0008	2007-05-11T01:22:55	600	326	243	7	90
JDWF0010	2007-05-11T01:37:36	600	328	250	6	90
JDWF0015	2007-05-11T02:30:28	600	335	274	3	90
JDWF0017	2007-05-11T02:46:03	600	337	282	2	90
JDWF0022	2007-05-11T03:37:23	600	345	305	-2	90
JDWF0024	2007-05-11T03:52:34	600	347	312	-3	90
JDWF0025	2007-05-11T04:04:15	600	348	318	-4	90
JDWF0026	2007-05-11T04:18:16	600	350	324	-5	90
JFQI0034	2007-06-20T23:37:43	600	11	183	9	90
JFQI0035	2007-06-20T23:49:40	600	12	188	9	90
JFQI0037	2007-06-21T00:05:42	600	14	196	10	90
JFQI0043	2007-06-21T01:05:08	600	23	224	9	90
JFQI0045	2007-06-21T01:19:53	600	25	230	8	90
JFQI0049	2007-06-21T01:59:44	600	31	249	7	90
JFQI0051	2007-06-21T02:14:04	600	33	256	6	90
JFQI0056	2007-06-21T03:12:27	600	41	282	2	90
JFQI0058	2007-06-21T03:28:22	600	43	290	0	90
JGGV0044	2007-07-06T21:53:49	600	10	7	-9	90
JGGV0045	2007-07-06T22:05:48	600	12	13	-9	90
JGGV0049	2007-07-06T22:36:19	600	16	27	-10	90
JGGV0052	2007-07-06T23:06:43	600	21	41	-9	90
JGGV0058	2007-07-07T00:02:07	600	29	67	-7	90
JGGV0062	2007-07-07T00:36:20	600	33	83	-5	90
JGGV0067	2007-07-07T01:20:25	600	40	103	-1	90
KPBB0028	2009-09-07T21:55:26	180	234	86	-4	-270
KPBB0034	2009-09-07T23:38:40	600	249	132	3	-270
KPCB0056	2009-09-08T23:43:16	600	93	81	-5	-270
KPCB0059	2009-09-09T00:24:09	600	99	100	-2	-180
KPFB0035	2009-09-09T20:22:05	600	268	296	-1	-270
KPFB0038	2009-09-09T20:59:06	600	273	313	-3	-180
KPFB0041	2009-09-09T21:33:50	600	278	329	-6	-270
KPFB0047	2009-09-09T22:27:46	600	286	353	-8	-270
KPIB0078	2009-09-12T23:43:39	600	187	230	9	-180
KPIB0081	2009-09-13T00:25:12	600	193	249	7	-270
KPJB0031	2009-09-13T21:33:57	600	12	116	1	-270
KPJB0033	2009-09-13T21:51:41	600	14	124	2	-270
KPJB0050	2009-09-14T01:30:31	600	45	226	9	-270

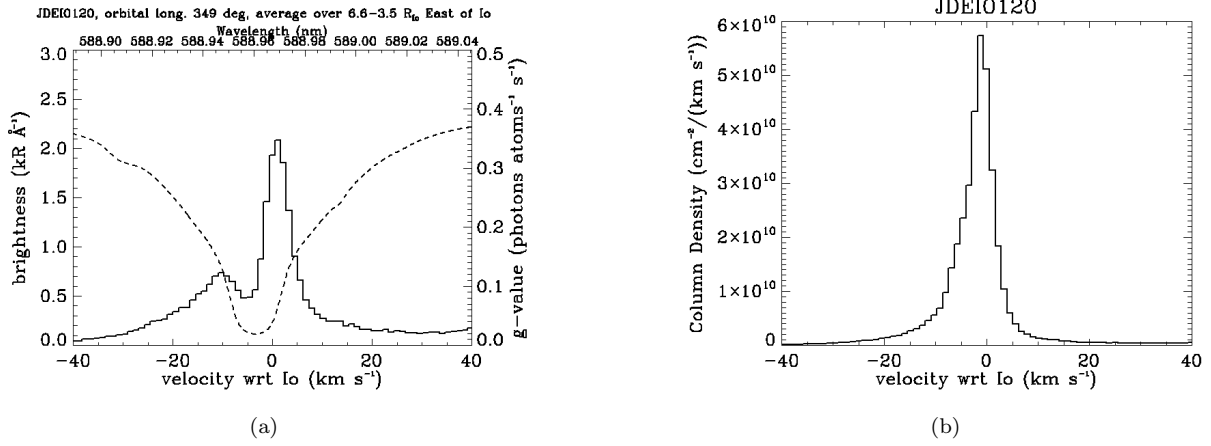


Figure 2. Left: spectrum of one Io observation (solid line) and the g-value used (dashed line) around the D2 emission line. Right: their ratio, which is the column density.

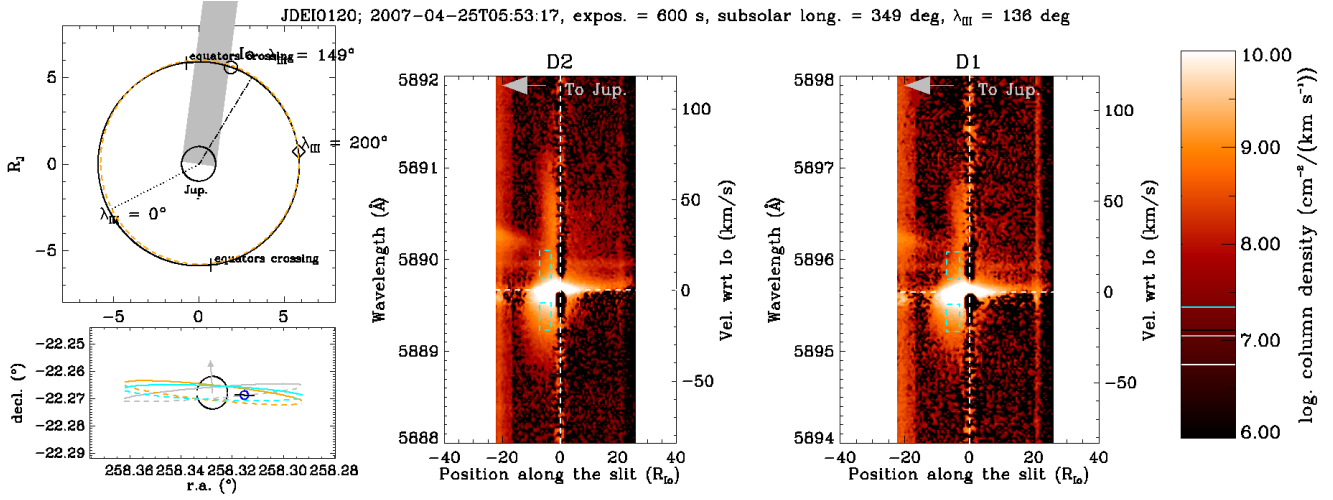


Figure 3. Composite image to put our 2D spectra in the observational perspective. The two right panels show our 2D Io spectra converted into column densities, in logarithmic color scale (D2 and D1, respectively). The region enclosed within the cyan dashed rectangles (7-22 km s⁻¹ and 3-7 Io radii) is used to compute the average source rate discussed in Section 5 and listed in Table 2. The gray arrows indicate the direction to Jupiter (towards right, in this case). The left panels show a simplified view of the geometry of the observations, from the celestial north pole (top) and from Earth (bottom), similar to Cremonese et al. (1992). Black solid circle on top (and gray on bottom) represents Io's orbit, in Jupiter's equatorial plane. Orange dashed circles on both top and bottom left panels represent Jupiter's magnetic equator at Io's distance, and include the tilt of 9.8° towards System III magnetic longitude $\lambda_{III} = 200^\circ$ and the offset of 0.12 R_J towards $\lambda_{III} = 149^\circ$. Cyan circle in bottom left panel represents the centrifugal equator, where the cold plasma ions reside. The arrow in the lower left panel indicates the rotation axis of Jupiter, and is black or gray if it points towards or away from the observer, respectively. Dashed lines in lower left panel indicate portions of the circles away from the observer. The blue circle and the small black line crossing it represent Io's disk and the spectrograph's slit, respectively. All objects in the two left panels are drawn to scale, except Io, for which the size has been magnified by 10. Corresponding images for the other observations can be found in the supplemental material.

232 to $\sim 75 \text{ km s}^{-1}$ is the stream of fast sodium atoms that
 233 feed the giant sodium nebula (e.g. Flynn et al. 1992).
 234 The feature modeled in this paper is the extended emis-
 235 sion blueshifted by few of tens of km s^{-1} with respect to
 236 Io, meaning these sodium atoms are moving towards the
 237 observer. The feature is seen here in the eastern half of
 238 the slit (left, in the figure), i.e. towards Jupiter.

239 4. MODELING THE EMISSION FEATURE

240 We applied our Monte Carlo model of sodium atom
 241 trajectories (Burger et al. 2014) to reproduce our obser-
 242 vations as closely as possible, by including the location
 243 and direction of ejection and the velocity distribution
 244 of ejected atoms. These parameters are constrained by
 245 our observations. The goal is to reproduce the emission
 246 feature and its temporal variability.

247 Figure 4 illustrates the change in time of the new fea-
 248 ture’s morphology at different orbital (or subsolar) lon-
 249 gitudes. This sequence shows that the blue-shifted fea-
 250 ture, more prominent towards the end of the observing
 251 run, early in the night is red-shifted by a similarly high
 252 speed ($> 10 \text{ km s}^{-1}$). The transition from red to blue
 253 shifts suggests that Na is ejected in a direction that is
 254 roughly perpendicular to the Io-observer line when the
 255 subsolar longitude is $\sim 330^\circ$ (between the 4th and the
 256 5th spectrum in Figure 4). This red-to-blue shift can
 257 then be explained by the changing observing geometry
 258 as Io orbits Jupiter. This peculiar behavior inspired
 259 our modeling approach. We first modeled the trajec-
 260 tories of the neutral sodium atoms (Section 4.1) and then
 261 found a plausible physical mechanism that can bring
 262 these sodium atoms at the location and with the speed
 263 we observe them (Section 4.1).
 264

265 4.1. Neutral sodium atoms trajectories

266 To simulate the observations we used the Monte Carlo
 267 model that is described in Burger et al. (2014). In this
 268 model, atoms are tracked under the forces of gravity and
 269 solar radiation pressure. The equations of motion are
 270 solved with a 5th order, adaptive step-size Runge-Kutta
 271 algorithm. Atoms are ejected at randomly selected times
 272 between the start and end of the model run so that the
 273 simulation contains a mixture of freshly released and
 274 older atoms. Loss processes include photoionization,
 275 electron-impact ionization, and charge exchange, though
 276 the atoms in the simulations shown below are mostly lost
 277 by leaving the small field of view. The observation ge-
 278 ometry was recreated using the SPICE toolkit (Acton
 279 1996).

280 We ran the model many times with different initial
 281 conditions in order to determine the direction and speed
 282 of Na that would reproduce the red-to-blue shift in Fig-
 283 ure 4. Sodium atoms are ejected radially in intervals

284 11.25° wide. The origin of the ejected atoms is labeled
 285 in Io’s West longitude, where 0° corresponds to the sub-
 286 Jupiter meridian and 90° points along Io’s orbital mo-
 287 tion (the “leading” direction). Speeds values from 4 to
 288 130 km s^{-1} were used, each with a narrow distribution
 289 (each bin being 10 m s^{-1} wide).

290 Each of the two free parameters we used to reproduce
 291 our observations affects only one aspect of the emis-
 292 sion feature. The ejection speed distribution affects the
 293 Doppler shift (wavelength dimension), while the ejection
 294 location affects the morphology of the emission feature
 295 (spatial direction). This is illustrated in Figure 5, where
 296 we show the effects of changing these parameters, com-
 297 pared to the nominal, best model.

298 We find that the best combination of parameters to re-
 299 produce our observations is a broad speed distribution,
 300 with ejection velocities relative to Io of $50\text{-}90 \text{ km s}^{-1}$,
 301 and a relatively narrow range of ejection location: 45-
 302 68° of Io West longitude, meaning an ejection from the
 303 subjovian/leading hemisphere. Models with the nomi-
 304 nal direction but lower speed (40 km s^{-1}) or higher speed
 305 (130 km s^{-1}) fail to match the magnitude of the Doppler
 306 shift, though they maintain the red-to-blue transition
 307 at a subsolar point of $\sim 330^\circ$ (left-right panels in Fig-
 308 ure 5). The mismatches in direction include one angular
 309 bin toward the leading direction and one bin toward the
 310 subjovian direction, and these both fail to reproduce the
 311 red-to-blue transition and the magnitude of the Doppler
 312 shift (top-down panels in Figure 5).

313 Figure 6 shows the best simulations compared to some
 314 of the observations. The rest of the data-model com-
 315 parison can be found in the movie in the Supplemental
 316 Material. The nominal model shown here (in both Fig-
 317 ure 5 and 6) includes speeds of 57 km s^{-1} and 90 km s^{-1} ,
 318 though lower speeds could be included without signifi-
 319 cantly changing the result. Figure 6 illustrates how our
 320 model can reproduce the shift in velocity relative to Io
 321 (from red, or positive, to blue, or negative) within the
 322 same amount of time (about 4 hours).

323 Figure 7 shows a top-down view of the nominal model
 324 of sodium trajectories near the beginning and end of the
 325 observing sequence. In this image, directions toward the
 326 observer (Earth, \oplus) and Jupiter (♃) are indicated. The
 327 red-to-blue shift is seen here as a change in ejection di-
 328 rection as seen from Earth. Also, it can be noted that
 329 the ejection direction is roughly halfway, in terms of
 330 degrees, between the leading direction and Jupiter di-
 331 rection.

332 4.2. Dust grains trajectories

333 Having found the characteristics of the sodium feature
 334 (speed distribution and direction), we need to identify

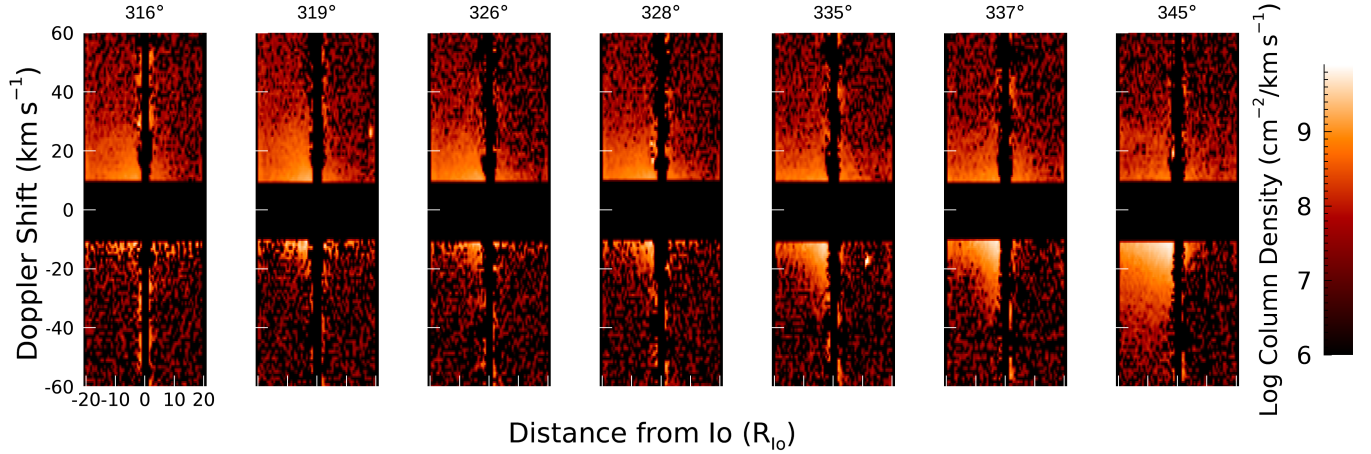


Figure 4. Observations taken in May 2007, calibrated in column density per unit velocity at different orbital (or subsolar) longitudes. Doppler velocities less than 10 km s^{-1} , which include the “banana cloud”, have been blacked out to highlight the feature, which transitions from red-shifted to blue-shifted in this 4-hour time span. Io’s orbital position is given as subsolar longitude and is indicated at the top of each plot. Io’s continuum has been carefully removed with the procedure discussed in the text.

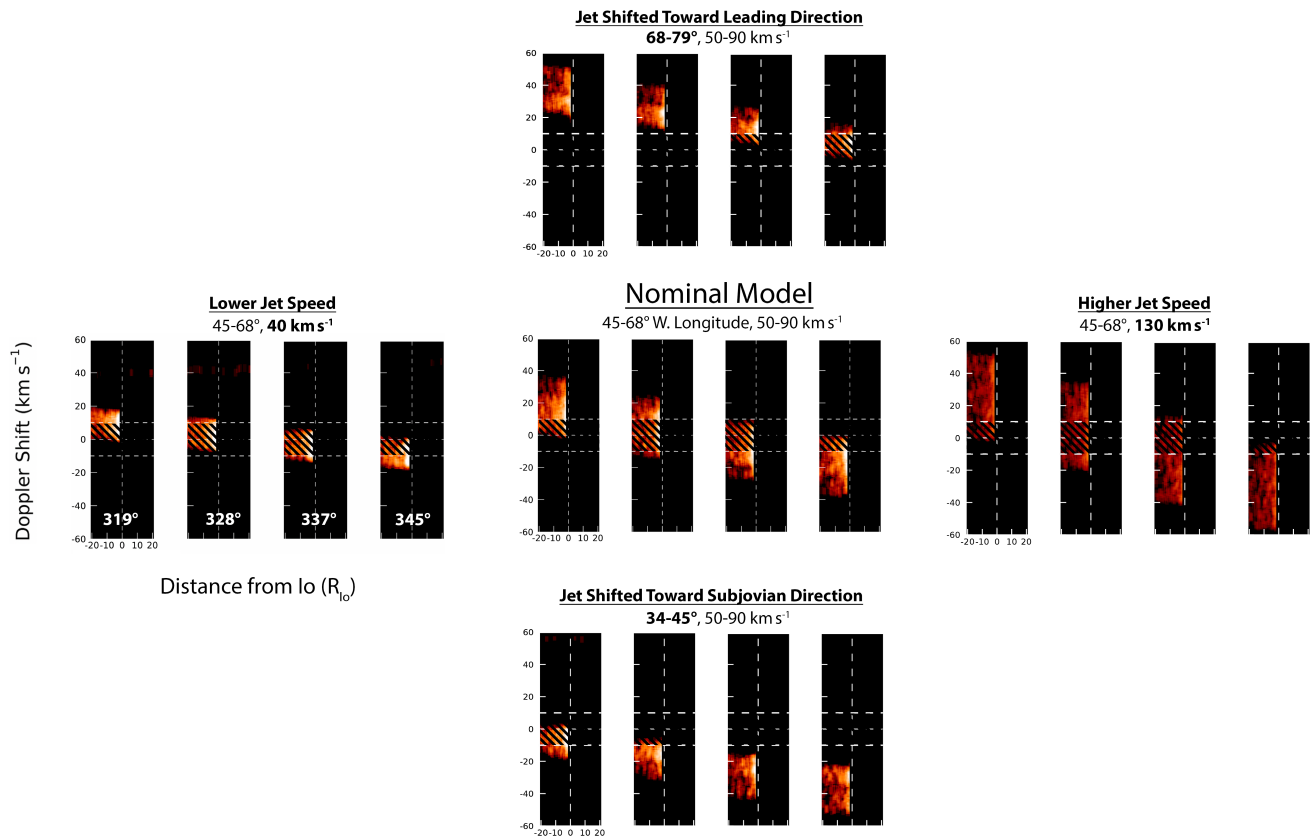


Figure 5. The simulation from the best model is shown at the center. The other four sub-panels show models with the right ejection direction but too low (left panel) or too fast (right panel) ejection speed, or models with the right ejection speed but wrong directions (top and bottom panels). Velocities within 10 km s^{-1} , marked by horizontal dashed lines, have been masked to leave out the main emission feature. The vertical dashed line represents the region of Io’s continuum.

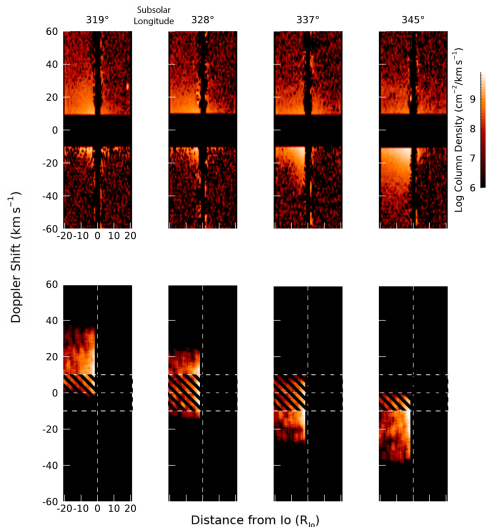


Figure 6. Comparison between four spectra in May 2007 (top panel) and their best fit model simulations (bottom panel). Note how the simulations are able to reproduce the shift in Doppler velocity, from positive relative velocities (moving away from the observer) to negative ones (moving towards the observer).

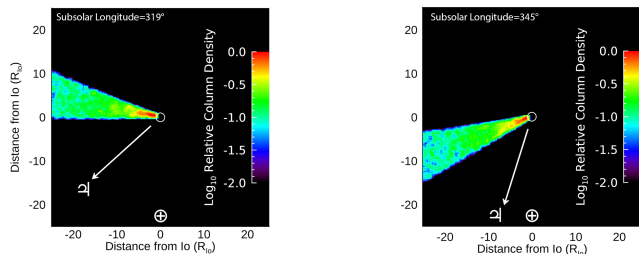


Figure 7. Top-down view of the model shown in Figure 6. The left panel shows the beginning of the observation sequence, when the Na is directed away from the observer to produce a red Doppler shift. The right panel shows the end of the sequence, when the Na is blue shifted. The white arrow points toward Jupiter, Earth is straight down.

a process that may bring sodium atoms at the location and speed observed. The direction of the blueshifted sodium feature (towards Jupiter) is consistent with negatively charged particles that move following Jupiter magnetosphere’s co-rotational electric field (e.g. Horányi et al. 1997). There are two possible candidates: sodium-bearing negative ions that are promptly neutralized and negatively charged Na-rich dust grains from which sodium atoms are liberated. In this section we discuss the latter, as many of the grains’ properties agree with our directional feature; at the end of Section 5.1 we briefly discuss the negative ions hypothesis.

Dust in the Jovian environment has been detected by multiple spacecraft: Ulysses (Grün et al. 1993), Galileo

(Grün et al. 1996), and Cassini (Postberg et al. 2006). All these observations are consistent with electrically charged dust grain of radius ~ 10 nm (Zook et al. 1996). The periodicity of the dust impact signal in Galileo data was one of the early indicators that Io, and not the gossamer rings, was the source of such dust grains (Graps et al. 2000). Subsequently, the Cosmic Dust Analyser (CDA) onboard Cassini was able to distinguish the composition of these grains. NaCl was the dominant species identified by CDA, followed by other components like Na_2SO_4 and K_2SO_4 (Postberg et al. 2006). This is in contrast with the main composition of Io’s atmosphere and neutral clouds, where NaCl, Na^+ , and Cl^+ are just trace species (NaCl fraction in composition is less than 1%, while the Na^+ and Cl^+ concentration in the torus is between 2 and 6%; Lellouch et al. 2003; Küppers & Schneider 2000). The inverse trend in composition for dust may be related to the process that ultimately ejects these particles in the first place, i.e. volcanic eruptions. Because of their high condensation temperature, NaCl and KCl are abundant condensates 20 min after outgassing from the vent, while sulphuric components, due to their lower condensation temperature, are still far from condensation (Zhang et al. 2004).

We performed simulations of the trajectory of negatively charged nanodust grains of various sizes. We assume that the dust particles 10nm in radii start with a circular Keplerian motion at Io’s orbit and an initial charge of 20 electric charge, corresponding to a surface potential of -3 V. The charging and dynamical evolution of nanometer-sized grains is modeled as described in Horányi et al. (1997). For individual dust grains, two equations are integrated simultaneously: the equation of motion and the grain charging equation. The equation of motion considers the gravity of Jupiter and the Lorentz forces acting on the grain from the co-rotating magnetosphere. The grain charging equation depends on plasma properties at the grain’s location and determines the grain charge-to-mass ratio, essential to calculate the Lorentz forces. Grains can be charged negatively or positively, depending on the plasma environment, and the charging begins almost instantaneously.

A top-down view of the trajectory of a negatively charged dust grain of radius 10 nm, as well as a positively charged one (same size), is shown in Figure 8. Figure 9 shows the direction, the relative speed and distance with respect to Io of a negatively charged dust grain of radius 10 nm. The gray circle in that figure represents the parameter space (both velocity and distance to Io) consistent with our observations. The dynamical evolution of charged nanoparticles largely depends on the grain charge polarity: the positively charged parti-

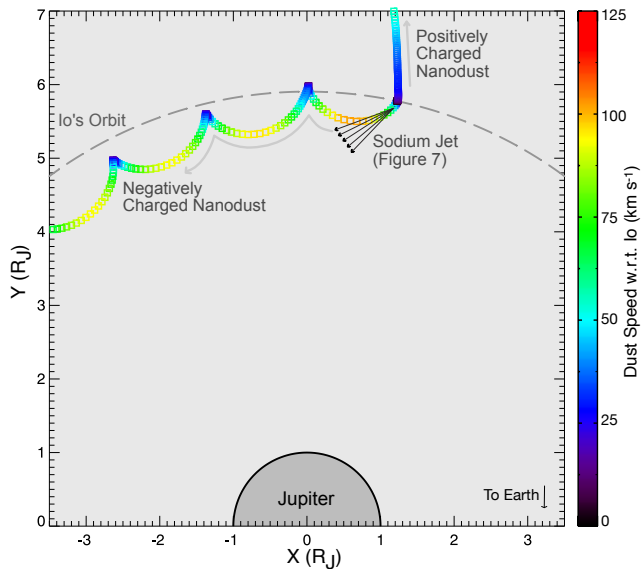


Figure 8. Top-down view of the trajectories of a negatively charged and a positively charged 10-nm-radius dust grain. $R_J = \text{Jupiter radius} \sim 70,000 \text{ km}$.

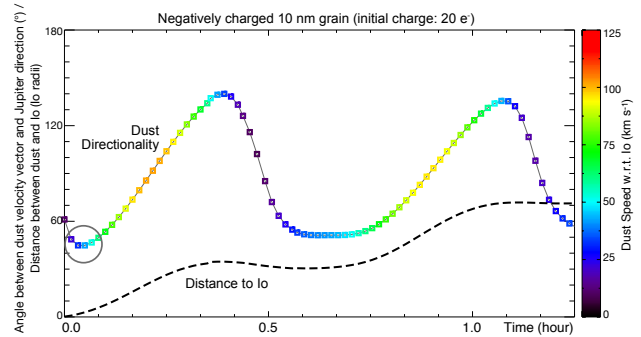


Figure 9. Simulation of trajectory of a negatively charged 10-nm-radius dust grain (of $20 e^-$ initial charge) moving under the influence the co-rotational electric field of Jupiter's magnetosphere. The line threading through the colored squares is the direction (angle), while the colored squares represent the velocity. The gray circle indicates the parameter space of the modeled neutral sodium atoms: speed range of $50\text{-}90 \text{ km s}^{-1}$ (cyan to yellow colors) and direction of $\sim 45^\circ$. The negatively charged particles have the right velocity at the right time to match our observations. The dashed line is the distance from Io and is also referred to the y axis (in Io radii) and that is also consistent with our data (Figure 4). Tick marks on the x axis are 5 minutes.

cle is accelerated away from Jupiter in almost a straight trajectory, while the negatively charged one exhibits a cycloidal motion along Io's orbit similar to pick-up ions. In general, negatively (positively) charged grains are accelerated towards (away from) Jupiter because of the outward-pointing co-rotating electric field (e.g. Horanyi et al. 1993). Within the first cycloid (within the first ~ 15 minutes), when the grain is within ~ 10 Io radii, both its direction and speed are comparable to the properties of the sodium jet. Grains of larger size (e.g. 100 nm), with a much smaller charge-to-mass ratio, are less accelerated by Lorentz forces compared to 10-nm-radius dust grains. Therefore, their velocity relative to Io is much smaller than the observed one. Similarly, much smaller particles (size < 10 nm) have a much smaller gyroradius and tend to stay much closer to Io (a couple of Io radii at most) than our sodium feature. We shall return to this point in the next Section.

5. DISCUSSION

Nanodust particles get charged at high altitude at Io by capture of ionospheric electrons or photoelectron production (Krüger et al. 2003a). Only the most energetic plumes are expected to bring grains to high altitudes so that they collect sufficient charge from ambient plasma to overcome Io's gravity (Johnson et al. 1980). Flandes (2004) showed that particles need to reach at least $\sim 400 \text{ km}$ altitude to be able to escape, and the flight time from vent to this height is 15-20 minutes.

Once they get charged, these nanodust particles follow trajectories that are determined by the corotational electric field of Jupiter's magnetosphere, in the radial direction. The dependence of dust trajectories on the highly variable magnetosphere in turn implies a certain variability in the expected dust flux with Jovian local time even if the dust ejection rate is constant. This variability, combined with the narrow field of view of our slit, might explain the variability seen in our dataset within a couple of hours (Figure 4). Most previous Io nanodust detection were carried out at distances further away from Io's orbit. In this respect, our observations probe a much closer region to Io than all previous dust measurements.

The spatial information of the observed Na jets also provides constraints on the dynamics of its possible dusty source. The observed Na speeds correspond roughly to $\sim 50 \text{ km s}^{-1}$, but grains in the dust model (10 nm in radius with $20 e^-$ initial charge) need to be accelerated for some distance before reaching those speeds, at least $7 R_{Io}$ as seen from Earth.

A dust grain with lower initial charge gets charged later, and thus farther away, and therefore its distance from Io would not match our observations. Only grains with proper charge-to-mass ratio can be sufficiently accelerated by the Lorentz forces and maintain a direction comparable to the observed sodium jet. To first order, regardless of the grain size, grains in the same plasma environment will be charged to roughly the same elec-

458 trostatic potential determined by the ambient plasma
 459 conditions. For a given electrostatic potential, the grain
 460 charge-to-mass ratio is inversely proportional to the
 461 square of the grain size. Negatively charged grains much
 462 larger than 10 nm have lower charge-to-mass ratio and
 463 would not be accelerated to the observed speed in the
 464 vicinity of Io. Negatively charged grains much smaller
 465 than 10 nm, on the other hand, have much smaller gy-
 466 roradius and will produce both red- and blue- shifted
 467 components in the vicinity of Io, which is also not con-
 468 sistent with the observation. The grain dynamics thus
 469 suggests that the sodium jet can only be produced by
 470 charged grains with radius ~ 10 nm. This is in good
 471 agreement with previous grain size estimate of the Jo-
 472 vian stream particles based on space dust instruments
 473 on board Galileo and Cassini spacecraft (Postberg et al.
 474 2006; Hsu et al. 2012).

475 It is possible to perform a rough estimate of the source
 476 rate from the spectra and compare it to the source rate
 477 from the neutral model. The sodium source rate r is
 478 the product of the peak column abundance, the vertical
 479 extent d of the emission, and the velocity v_{\perp} perpen-
 480 dicular to the observer’s line of sight (Schneider et al.
 481 1991):

$$r = d \cdot v_{\perp} \cdot \int_{v_1}^{v_2} n(v) dv \quad (3)$$

482 In the above formula, we used Io’s diameter as verti-
 483 cal extent d of our feature; n is the column density per
 484 unit velocity averaged between 3.0 and 7.0 R_{Io} and the
 485 integral is performed between $v_1 = 7$ and $v_2 = 22$ km
 486 s^{-1} relative to Io, where the blueshifted feature is more
 487 prominent. Finally, the velocity perpendicular to the
 488 observer’s line of sight is defined as $v_{\perp} = v_{los} \cdot \tan(\theta)$,
 489 where v_{los} is the line-of-sight velocity (the one our spec-
 490 troscopic observations are sensitive to) and θ is the angle
 491 between our line of sight and the jet (we assume our di-
 492 rectional feature, or “jet”, to be the axis of the cone of
 493 sodium atoms – see Figure 7). This angle is necessarily
 494 taken out of our modeling, since with spectroscopic ob-
 495 servations we can only measure the radial (line of sight)
 496 velocity and have no information on the true orientation
 497 of the sodium feature. For each spectrum, we average
 498 the D2 and the D1 source rates and report these num-
 499 bers in Table 2. The median of the resulting sodium
 500 source rates is 7.0×10^{25} Na s^{-1} from the data, corre-
 501 sponding to 2.7 kg s^{-1} . The source rate from the neutral
 502 model is somehow greater (2.6×10^{26} Na s^{-1} , correspond-
 503 ing to 10.0 kg s^{-1}), but this was derived assuming a wide
 504 “jet” (30° in the vertical direction). A narrower feature
 505 would require proportionally less sodium.

5.1. Sputtering of Na from nanodust grains

Table 2. Sodium source rate for the emission feature dis-
 cussed in this paper. The data source rate is the average of
 the source rates from the D2 and D1 emission lines). Model
 source rates for some of the April 2007 observations are not
 available because the emission feature was not well defined.

filename	data source rate (s^{-1})	model source rate (s^{-1})
JDEI0119	7.0×10^{25}	1.6×10^{26}
JDEI0120	1.1×10^{26}	2.6×10^{26}
JDWF0002	1.4×10^{25}	5.8×10^{25}
JDWF0004	2.8×10^{25}	9.2×10^{25}
JDWF0008	4.6×10^{25}	1.4×10^{26}
JDWF0010	7.0×10^{25}	2.1×10^{26}
JDWF0015	2.3×10^{26}	2.9×10^{26}
JDWF0017	1.7×10^{26}	2.7×10^{26}
JDWF0022	9.8×10^{25}	2.8×10^{26}
JDWF0024	7.7×10^{25}	3.0×10^{26}
JDWF0025	6.9×10^{25}	2.2×10^{26}

507 For the dust hypothesis to work, we need a mechanism
 508 that releases sodium atoms from these nanodust grains.
 509 Possible processes include photon-stimulated desorption
 510 (PSD), electron-stimulated desorption (ESD), or ion
 511 sputtering. The first two have too low a source rate.
 512 From experiments of PSD of Na from surfaces that sim-
 513 ulate the lunar silicates (Yakshinskiy & Madey 1999),
 514 scaling the solar flux to Jupiter’s distance, and taking
 515 into account our derived distribution of dust grains, the
 516 source rate from PSD is 10^9 s^{-1} . The same authors also
 517 showed that electron-stimulated desorption has an only
 518 slightly higher cross section compared to PSD. The other
 519 mechanism, ion sputtering, gives higher source rates, al-
 520 though there are several uncertainties that affect the
 521 calculation of the rate. First, an absolute value for
 522 sputtering yield of sodium atoms has only been mea-
 523 sured on Na_2S : Chrisney et al. (1988) report a sputtering
 524 yield of 0.1 and 0.2 Na_2S ion $^{-1}$ from O^+ and S^+ ions,
 525 respectively. The molecules of interest in our case are
 526 sodium chloride (NaCl) and sodium sulfate (Na_2SO_4),
 527 given that these were the compositions of the Na-bearing
 528 dust grains detected by Cassini CDA (Postberg et al.
 529 2006). Sodium sputtering yield for NaCl has been esti-
 530 mated by Johnson (2000) to be ~ 1.0 Na ion $^{-1}$, assum-
 531 ing that NaCl has the same atomic ejection efficiency
 532 as Na_2S . Sodium sputtering yield for Na_2SO_4 has only
 533 been reported as a relative value: it is 100-1000 times
 534 greater than the sputtering yield for NaS (Wiens et al.
 535 1997). Assuming the absolute sputtering yield of NaS
 536 to be the same as that of Na_2S , we can estimate the
 537 Na sputtering yield from Na_2SO_4 to be 100-1000 times
 538 greater than that of NaCl, or 100-1000 Na ion $^{-1}$. The

flux Φ of precipitating ions responsible for the sputtering (mostly S^+ and O^+) can be calculated by multiplying the velocity of the ions (co-rotation, or 57 km s^{-1}) by the density of these heavy ions close to Io, or about 1500 cm^{-3} (Dougherty et al. 2017). We obtain $\Phi = 8.6 \times 10^9 \text{ cm}^{-2} \text{ s}^{-1}$.

The second uncertainty is the dust available for sputtering. Over the course of the 7-year mission and from a distance between 13 and $400 R_J$ from Io, the Galileo Dust Detector System (DDS) measured dust production rates at Io between 10^{-3} and 10^2 kg s^{-1} (with an average value between 0.1 and 1.0 kg s^{-1}), possibly correlated to volcanic eruptions at Io (Figure 2 of Krüger et al. 2003b).

With these numbers, we can estimate the number of Na atoms sputtered by nanodust grains and compare it to our observed sodium production rate. We start by assuming a dust production rate of 1 kg s^{-1} , the upper value of the average range reported by Krüger et al. (2003b). Assuming a spherical shape and a density of 1.5 g cm^{-3} (Krüger et al. 2003b), this corresponds to 1.6×10^{20} grains s^{-1} of radius 10 nm . We now multiply this number by the time it takes for the dust grains to reach the point where we do see sodium emission, or 0.05 hours (from Figure 9), to get $N_{grains} = 2.9 \times 10^{22}$. The total area available for sputtering will be $N_{grains} \cdot A \cdot c$, where A is the area of a 10-nm -radius spherical nanodust grain, and c the concentration of either NaCl (90%) or Na_2SO_4 (10%), from Cassini CDA measurements (Postberg et al. 2006). These areas are $3.2 \times 10^{11} \text{ cm}^{-2}$ and $3.6 \times 10^{10} \text{ cm}^{-2}$ for NaCl and Na_2SO_4 , respectively. Multiplying them by the corresponding sputtering yields Y and the heavy ion flux, we get the sodium production rate for sputtering s :

$$s = N_{grains} \cdot A \cdot c \cdot \Phi \cdot Y \quad (4)$$

We obtain $2.8 \times 10^{21} \text{ Na s}^{-1}$ from NaCl, and $3.1 \times 10^{22} \text{ Na s}^{-1}$ from Na_2SO_4 from 1 kg s^{-1} of dust material.

These numbers are between 3 and 4 orders of magnitude lower than our inferred rate of $7.0 \times 10^{25} \text{ s}^{-1}$ (from the observations). They can be reconciled with our values if we assume some combination of the highest estimate for dust production rate from Galileo (100 kg s^{-1}), the highest estimate for the sputtering yield of Na from Na_2SO_4 (1000 Na ion^{-1}), and a surface area for porous particles which is ~ 10 times higher than the spherical area (this is the case for micron-sized lunar regolith particles; Taylor & Meek 2004). Additionally, the dust production rates from Galileo should be considered a lower limit, as dust is likely to undergo other destruction processes (not included in the calculations of Krüger et al. 2003b) between Io and the distance at

which grains were detected by Galileo (between 13 and $400 R_J$ from Io). This is particularly true if some ejected dust has a more volatile composition than NaCl. Finally, it is not clear how the ion sputtering experiments, performed on flat surfaces, would change if the target is composed of nm-sized porous surfaces. To further investigate the discrepancy, a detailed calculation of the release of Na from dust particles and full treatment of dust destruction in Jupiter's highly complicated plasma environment would be required, and these are outside the scope of this paper.

We note that the new sodium feature was most prominent when Io was within 5° of the magnetic equator (Table 1). The bulk of the Io plasma torus is confined in the centrifugal equator, which is very close to the magnetic one. The plasma environment of that region (high plasma electron density and low electron temperature; Meyer-Vernet et al. 1995) is consistent with the negative grain charge polarity inferred from the trajectory simulation. In addition, the sputtering erosion responsible to release sodium atoms from dust surfaces is also higher at low magnetic latitudes because of the higher ion density. Our results thus indicate an indirect pathway to deliver sodium atoms, and likely other species, from Io to the Neutral Clouds (and ultimately to the magnetosphere) by sputtering from dust surfaces.

We conclude this section by evaluating and discarding another possible candidate, mentioned in Section 4.2, that is a population of negative ions formed inside Io's plumes. In this case, the most likely process to create these ions is three-body electron attachment. The most likely species to undergo this process is NaSO_4 , a radical species with a substantial electron affinity and the highest rate coefficient among several Na-bearing species. The negative ions would then release the neutral sodium atoms we observe following electron detachment. The concentration of NaSO_4 inside Io's plumes is unknown, but to match our observed source rate per unit volume, a density similar to that of potassium would be required, or 9 orders of magnitude greater than the expected concentration of Na_2SO_4 inside Io's plumes (Moses et al. 2002). For this reason, we favor the hypothesis of ion sputtering from negatively charged dust nanograins as the most plausible source of our new sodium emission feature.

6. CONCLUSIONS

We have performed Monte Carlo simulation of sodium atoms under the influence of Io's gravity and solar radiation pressure to explain an unusual Jupiter-oriented feature (Schneider et al. 2008) we detected in our high-resolution spectra of Io's sodium Neutral Clouds from

640 the TNG telescope. This feature is directed towards
 641 Jupiter and is rapidly variable in time. The best model
 642 is the one that has the sodium atoms ejected in the
 643 leading-sub/Jovian hemisphere of Io (45–68° West lon-
 644 gitude) with a broad velocity distribution (50–90 km
 645 s⁻¹). We propose that the mechanism most likely re-
 646 sponsible for creating sodium atoms with that orienta-
 647 tion and that speed is sputtering of Na from Na-bearing
 648 molecules (NaCl or Na₂SO₄, both detected near Jupiter
 649 by Cassini CDA) attached to negatively charged dust
 650 grains (10 nm in radius) that move under the influence
 651 of the co-rotational electric field of Jupiter’s magneto-
 652 sphere. This is consistent with modeling of trajectories
 653 of negatively charged nanodust grains, which present the
 654 right velocity and orientation consistent with our ob-
 655 servations and our sodium model. The median sodium
 656 source rate inferred from our observations is 7.0×10^{25}
 657 Na s⁻¹, to be compared with the theoretical estimate
 658 from ion sputtering of Na from NaCl or Na₂SO₄ be-
 659 tween 5.5×10^{21} Na s⁻¹ and 6.2×10^{26} Na s⁻¹, depending
 660 on the choice of several uncertain parameters, such as
 661 the sputtering yield, the dust production rate at Io, and
 662 surface area available to sputtering. We point out the
 663 need for detailed calculations of the release of Na from
 664 dust particles and full treatment of dust destruction in
 665 Jupiter’s highly complicated plasma environment.

666 Our results uncover a new mechanism by which Io’s
 667 sodium Neutral Clouds are replenished, and highlight
 668 the need for future observing campaigns to better con-
 669 strain the escape rate of sodium atoms produced at Io
 670 by this mechanism, before the arrival of Europa Clip-
 671 per spacecraft, whose dust counter will be able to study
 672 the dust population in the Jupiter environment at much
 673 closer range than any other spacecraft so far.

674 ACKNOWLEDGEMENTS

675 This work has been supported by NASA Solar Sys-
 676 tem Workings grant 80NSSC18K0008, NSF’s Planetary
 677 Astronomy Program, and the Astronomy Department
 678 and CISAS of University of Padua, through a contract
 679 by the Italian Space Agency (ASI). Cesare Grava wishes
 680 to thank Rosemary M. Killen for providing the g-values
 681 used in this work, and Jane L. Fox and John M. C.
 682 Plane for insightful discussions on negative ions chem-
 683 istry. Based on observations made with the Italian *Tele-*
 684 *scopio Nazionale Galileo* (TNG) operated by the *Fun-*
 685 *dación Galileo Galilei* of the *Istituto Nazionale di As-*
 686 *trofisica* at the *Observatorio del Roque de los Mucha-*
 687 *chos* (La Palma, Canary Islands, Spain). Files for ob-
 688 servations in 2009 are available on the archive of the
 689 TNG telescope, at <http://archives.ia2.inaf.it/tng>. Files
 690 for observations in 2007 can be requested to the corre-
 691 sponding author.

REFERENCES

- 692 Acton, C. H. 1996, *Planet. Space Sci.*, 44, 65,
 693 doi: [10.1016/0032-0633\(95\)00107-7](https://doi.org/10.1016/0032-0633(95)00107-7)
- 694 Bagenal, F., & Dols, V. 2020, *Journal of Geophysical*
 695 *Research (Space Physics)*, 125, e27485,
 696 doi: [10.1029/2019JA027485](https://doi.org/10.1029/2019JA027485)
- 697 Brown, R. A. 1974, in *IAU Symposium*, Vol. 65,
 698 *Exploration of the Planetary System*, ed. A. Woszczyk &
 699 C. Iwaniszewska, 527–531
- 700 Brown, R. A., Goody, R. M., Murcray, F. J., & Chaffee,
 701 F. H., J. 1975, *ApJL*, 200, L49, doi: [10.1086/181894](https://doi.org/10.1086/181894)
- 702 Brown, R. A., & Schneider, N. M. 1981, *Icarus*, 48, 519,
 703 doi: [10.1016/0019-1035\(81\)90061-0](https://doi.org/10.1016/0019-1035(81)90061-0)
- 704 Brown, R. A., & Yung, Y. L. 1976, in *Jupiter*, 1102–1145
- 705 Burger, M. H., Killen, R. M., McClintock, W. E., et al.
 706 2014, *Icarus*, 238, 51, doi: [10.1016/j.icarus.2014.04.049](https://doi.org/10.1016/j.icarus.2014.04.049)
- 707 Chrisey, D. B., Johnson, R. E., Boring, J. W., & Phipps,
 708 J. A. 1988, *Icarus*, 75, 233,
 709 doi: [10.1016/0019-1035\(88\)90003-6](https://doi.org/10.1016/0019-1035(88)90003-6)
- 710 Cremonese, G., Thomas, N., Barbieri, C., & Pernechele, C.
 711 1992, *A&A*, 256, 286
- 712 Dougherty, L. P., Bodisch, K. M., & Bagenal, F. 2017,
 713 *Journal of Geophysical Research (Space Physics)*, 122,
 714 8257, doi: [10.1002/2017JA024053](https://doi.org/10.1002/2017JA024053)
- 715 Flandes, A. 2004, *Geophys. Res. Lett.*, 31, L16802,
 716 doi: [10.1029/2004GL020046](https://doi.org/10.1029/2004GL020046)
- 717 Flynn, B., Mendillo, M., & Baumgardner, J. 1992, *Icarus*,
 718 99, 115, doi: [10.1016/0019-1035\(92\)90176-8](https://doi.org/10.1016/0019-1035(92)90176-8)
- 719 Goldberg, B. A., Garneau, G. W., & Lavoie, S. K. 1984,
 720 *Science*, 226, 512, doi: [10.1126/science.226.4674.512](https://doi.org/10.1126/science.226.4674.512)
- 721 Graps, A. L., Grün, E., Svedhem, H., et al. 2000, *Nature*,
 722 405, 48, doi: [10.1038/35011008](https://doi.org/10.1038/35011008)
- 723 Grava, C., Schneider, N. M., Leblanc, F., et al. 2014,
 724 *Journal of Geophysical Research (Planets)*, 119, 404,
 725 doi: [10.1002/2013JE004504](https://doi.org/10.1002/2013JE004504)
- 726 Grün, E., Zook, H. A., Baguhl, M., et al. 1993, *Nature*, 362,
 727 428, doi: [10.1038/362428a0](https://doi.org/10.1038/362428a0)
- 728 Grün, E., Baguhl, M., Hamilton, D. P., et al. 1996, *Nature*,
 729 381, 395, doi: [10.1038/381395a0](https://doi.org/10.1038/381395a0)
- 730 Horányi, M., Grün, E., & Heck, A. 1997,
 731 *Geophys. Res. Lett.*, 24, 2175, doi: [10.1029/97GL01539](https://doi.org/10.1029/97GL01539)

- 732 Horanyi, M., Morfill, G., & Grun, E. 1993, *Nature*, 363,
733 144, doi: [10.1038/363144a0](https://doi.org/10.1038/363144a0)
- 734 Hsu, H.-W., Krüger, H., & Postberg, F. 2012, in *Nanodust*
735 *in the Solar System: Discoveries and Interpretations*
736 (Springer), 77–117
- 737 Hunten, D. M., Morgan, T. H., & Shemansky, D. E. 1988,
738 *The Mercury atmosphere.*, ed. F. Vilas, C. R. Chapman,
739 & M. S. Matthews, 562–612
- 740 Hunten, D. M., Roach, F. E., & Chamberlain, J. W. 1956,
741 *Journal of Atmospheric and Terrestrial Physics*, 8, 345,
742 doi: [10.1016/0021-9169\(56\)90111-8](https://doi.org/10.1016/0021-9169(56)90111-8)
- 743 Johnson, R. E. 2000, *Icarus*, 143, 429,
744 doi: [10.1006/icar.1999.6327](https://doi.org/10.1006/icar.1999.6327)
- 745 Johnson, T. V., Morfill, G., & Grun, E. 1980,
746 *Geophys. Res. Lett.*, 7, 305,
747 doi: [10.1029/GL007i005p00305](https://doi.org/10.1029/GL007i005p00305)
- 748 Killen, R., Shemansky, D., & Mouawad, N. 2009, *ApJS*,
749 181, 351, doi: [10.1088/0067-0049/181/2/351](https://doi.org/10.1088/0067-0049/181/2/351)
- 750 Krüger, H., Horányi, M., & Grün, E. 2003a,
751 *Geophys. Res. Lett.*, 30, 1058,
752 doi: [10.1029/2002GL015920](https://doi.org/10.1029/2002GL015920)
- 753 Krüger, H., Geissler, P., Horányi, M., et al. 2003b,
754 *Geophys. Res. Lett.*, 30, 2101,
755 doi: [10.1029/2003GL017827](https://doi.org/10.1029/2003GL017827)
- 756 Küppers, M., & Schneider, N. M. 2000,
757 *Geophys. Res. Lett.*, 27, 513, doi: [10.1029/1999GL010718](https://doi.org/10.1029/1999GL010718)
- 758 Lellouch, E., Paubert, G., Moses, J. I., Schneider, N. M., &
759 Strobel, D. F. 2003, *Nature*, 421, 45,
760 doi: [10.1038/nature01292](https://doi.org/10.1038/nature01292)
- 761 Mendillo, M., Baumgardner, J., Flynn, B., & Hughes, W. J.
762 1990, *Nature*, 348, 312, doi: [10.1038/348312a0](https://doi.org/10.1038/348312a0)
- 763 Meyer-Vernet, N., Moncuquet, M., & Hoang, S. 1995,
764 *Icarus*, 116, 202, doi: [10.1006/icar.1995.1121](https://doi.org/10.1006/icar.1995.1121)
- 765 Moses, J. I., Zolotov, M. Y., & Fegley, B. 2002, *Icarus*, 156,
766 107, doi: [10.1006/icar.2001.6759](https://doi.org/10.1006/icar.2001.6759)
- 767 Nash, D. B., Yoder, C. F., Carr, M. H., Gradie, J., &
768 Hunten, D. M. 1986, *Io*, ed. J. A. Burns & M. S.
769 Matthews, 629–688
- 770 Postberg, F., Kempf, S., Srama, R., et al. 2006, *Icarus*, 183,
771 122, doi: [10.1016/j.icarus.2006.02.001](https://doi.org/10.1016/j.icarus.2006.02.001)
- 772 Schneider, N. M., & Bagenal, F. 2007, *Io's neutral clouds,*
773 *plasma torus, and magnetospheric interaction*, ed.
774 R. M. C. Lopes & J. R. Spencer, 265,
775 doi: [10.1007/978-3-540-48841-5_11](https://doi.org/10.1007/978-3-540-48841-5_11)
- 776 Schneider, N. M., Grava, C., & Barbieri, C. 2008, in
777 *AAS/Division for Planetary Sciences Meeting Abstracts*
778 *#40, AAS/Division for Planetary Sciences Meeting*
779 *Abstracts*, 59.09
- 780 Schneider, N. M., Trauger, J. T., Wilson, J. K., et al. 1991,
781 *Science*, 253, 1394, doi: [10.1126/science.253.5026.1394](https://doi.org/10.1126/science.253.5026.1394)
- 782 Taylor, L. A., & Meek, T. T. 2004, in *International Lunar*
783 *Conference 2003*, ed. S. M. Durst, C. T. Bohannon, C. G.
784 Thomason, M. R. Cerney, & L. Yuen, Vol. 108, 109
- 785 Trafton, L. 1975, *ApJL*, 202, L107, doi: [10.1086/181991](https://doi.org/10.1086/181991)
- 786 Trafton, L., & Macy, W., J. 1977, *ApJ*, 215, 971,
787 doi: [10.1086/155433](https://doi.org/10.1086/155433)
- 788 Trafton, L., & Macy, W. 1978, *Icarus*, 33, 322,
789 doi: [10.1016/0019-1035\(78\)90152-5](https://doi.org/10.1016/0019-1035(78)90152-5)
- 790 Trafton, L., Parkinson, T., & Macy, W., J. 1974, *ApJL*,
791 190, L85, doi: [10.1086/181512](https://doi.org/10.1086/181512)
- 792 Wiens, R. C., Burnett, D. S., Calaway, W. F., et al. 1997,
793 *Icarus*, 128, 386, doi: [10.1006/icar.1997.5758](https://doi.org/10.1006/icar.1997.5758)
- 794 Wilson, J. K., & Schneider, N. M. 1994, *Icarus*, 111, 31,
795 doi: [10.1006/icar.1994.1131](https://doi.org/10.1006/icar.1994.1131)
- 796 —. 1999, *J. Geophys. Res.*, 104, 16567,
797 doi: [10.1029/1999JE900017](https://doi.org/10.1029/1999JE900017)
- 798 Yakshinskiy, B. V., & Madey, T. E. 1999, *Nature*, 400, 642,
799 doi: [10.1038/23204](https://doi.org/10.1038/23204)
- 800 Zhang, J., Goldstein, D. B., Varghese, P. L., et al. 2004,
801 *Icarus*, 172, 479, doi: [10.1016/j.icarus.2004.06.016](https://doi.org/10.1016/j.icarus.2004.06.016)
- 802 Zook, H. A., Grun, E., Baguhl, M., et al. 1996, *Science*,
803 274, 1501, doi: [10.1126/science.274.5292.1501](https://doi.org/10.1126/science.274.5292.1501)